Microporous and Mesoporous Materials 335 (2022) 111818

Contents lists available at ScienceDirect

Microporous and Mesoporous Materials

journal homepage: www.elsevier.com/locate/micromeso

3D-printed activated carbon for post-combustion CO_2 capture

Lucas F.A.S. Zafanelli [a,b,*], Adriano Henrique [a,b], Hendryk Steldinger [c], Jose L. Diaz de Tuesta [a], Jan Gläsel [c], Alírio E. Rodrigues [b], Helder T. Gomes [a,**], Bastian J.M. Etzold [c,***], José A. C. Silva [a,****]

[a] Centro de Investigação de Montanha (CIMO), Instituto Politécnico de Bragança, Campus Santa Apolónia, 5300-253, Bragança, Portugal
[b] Laboratory of Separation and Reaction Engineering (LSRE), Associate Laboratory LSRE/LCM, Department of Chemical Engineering, Faculty of Engineering, University of Porto, 4099-002, Porto, Portugal
[c] Technical University of Darmstadt, Department of Chemistry, Ernst-Berl-Institut für Technische und Makromolekulare Chemie, 64287, Darmstadt, Germany

ARTICLE INFO

Keywords:
3D printed monoliths
Fixed bed adsorption
Multi-component adsorption
Numerical modeling
Post-combustion CO_2 capture

ABSTRACT

The applicability of 3D-printed activated carbons for their use to CO_2 capture in post-combustion streams and the influence of activation conditions on CO_2 uptake and CO_2 to N_2 selectivity were studied. For two monoliths with the same open cellular foam geometry but low and high burnoff during activation, a series of fixed-bed breakthrough adsorption experiments under typical post-combustion conditions, in a wide range of temperature (313 and 373 K), and partial pressure of CO_2 up to 120 kPa were carried out. It is shown that the higher burnoff during activation of the 3D printed carbon enhances the adsorption capacity of CO_2 and N_2 due to the increased specific surface area with sorption uptakes that can reach 3.17 mol/kg at 313 K and 120 kPa. Nevertheless, the lower burnoff time on monolith 1 leads to higher selectivity of CO_2 over N_2, up to 18 against 10 on monolith 2, considering a binary interaction to a mixture of CO_2/N_2 (15/85 vol%) at 313 K. The single and multicomponent adsorption equilibrium is conveniently described through the dual-site Langmuir isotherm model, while the breakthrough curves simulated using a dynamic fixed-bed adsorption linear driving force model. Working capacities for the 3D printed carbon with lower burnoff time lead to the best results, varying of 0.15–1.1 mol/kg for the regeneration temperature 300–390 K. Finally, consecutive adsorption-desorption experiments show excellent stability and regenerability for both 3D printed activated carbon monoliths and the whole study underpins the high potential of these materials for CO_2 capture in post-combustion streams.

1. Introduction

CO_2 capture from post-combustion streams in coal-fired power plants can play an important role to mitigate global warming [1]. This carbon source is responsible at least for 73% of annual energy sector emissions [2]. Therefore, to achieve the International Panel on Climate Change (IPCC) target by keeping the global warming average less than 2 °C, great efforts have been made towards the decrease of penalty energy and increase CO_2 recovery on actual capture technologies [1].

The chemical absorption technology with monoethanolamine still is the most widely used for CO_2 capture [1]. However, its regeneration step requires high energy consumption which makes the process expensive [3]. Among other technologies, namely cryogenic [4] and membrane [5], adsorption processes are recognized as an attractive and costly-efficient alternative for CO_2 capture on post-combustion applications [1,6,7]. Additionally, the availability of several solid-based materials and many regeneration steps (temperature, pressure, vacuum, and electrical swing adsorption) makes the optimization of the adsorption processes to ensure acceptable footprint and cost versatile.

Commonly solid-based materials used to adsorb CO_2 are zeolites (13X, 5A, and 4A) [8–10], activated carbon [11], and metal-organic frameworks [12]. These materials are synthesized into a powder form

* Corresponding author. Centro de Investigação de Montanha (CIMO), Instituto Politécnico de Bragança, Campus Santa Apolónia, 5300-253, Bragança, Portugal.
** Corresponding author. Centro de Investigação de Montanha (CIMO), Instituto Politécnico de Bragança, Campus Santa Apolónia, 5300-253, Bragança, Portugal.
*** Corresponding author. Technical University of Darmstadt, Department of Chemistry, Ernst-Berl-Institut für Technische und Makromolekulare Chemie, 64287, Darmstadt, Germany.
**** Corresponding author. Centro de Investigação de Montanha (CIMO), Instituto Politécnico de Bragança, Campus Santa Apolónia, 5300-253, Bragança, Portugal.
E-mail addresses: zafanelli@ipb.pt (L.F.A.S. Zafanelli), htgomes@ipb.pt (H.T. Gomes), bastian.etzold@tu-darmstadt.de (B.J.M. Etzold), jsilva@ipb.pt (J.A.C. Silva).

https://doi.org/10.1016/j.micromeso.2022.111818
Received 11 November 2021; Received in revised form 24 February 2022; Accepted 7 March 2022
Available online 13 March 2022

and transformed into pellets or beads before being applied to adsorption systems. However, when using pellets or beads on a system that needs high gas velocities, e.g. systems with short cycle times, the process tends to suffer from higher pressure-drop [13]. Besides, package-bed with pellets or beads exhibit an inhomogeneous temperature along the bed due to low electrical conductivity, as well as, barriers to heat transfer caused by contact between particles [14,15]. The resulting maldistribution of temperature is a disadvantage on cycles that work with regeneration step based on temperatures, like Temperature or Electrical Swing Adsorption (TSA and ESA).

Alternatively to conventional beads/pellets configurations, novel adsorbent structures have been developed to overcome the main issues related to packaging beds [3,14,16–21]. Monolith presents an entirely non-particulate structure and open channels that can reduce the pressure drop on the system over higher flowrates [22]. Additionally, the temperature distribution in a monolith is nearly uniform due to the ease heat dissipation of throughout its structure, as there is no thermal resistance between the particles [14,15]. Among other advantages, the monolith can be designed with a high level of freedom to achieve better performance towards CO_2 capture. For example, Zhao et al. [23] synthesized a hybrid activated carbon (from phenolic resin) and zeolite NaUSY monolith with excellent electrical properties for ESA applications. They have shown a great reduction (from 73% to 18%) in energy loss in the contact between the hybrid adsorbent surface and the copper electrode. The reduction of energy loss allows a quick increase of temperature in the regeneration step by heating the adsorbent and, hence, operational cost reduction. Regufe et al. [24] have reported a 3D-printed honeycomb monolith composed of zeolite 13X, activated carbon, and binder especially design for the application in the ESA process. The material showed a fast increase in temperature, e.g. it achieved 377 K in 180 s from room temperature. A short cyclic adsorption process submitted at humidity conditions was evaluated by Verougstraete et al. [25] using a new honeycomb carbon monolith for CO_2 capture from flue gases. It was shown that the monolith can CO_2 capture at very high gas flow rates (up to 5 LPM which corresponds to an interstitial gas velocity equal to 3.23 m/s) and the presence of humidity did not strongly affect the capacity of adsorption as compared to 13X zeolite.

These results suggest that monolith has the potential to be a promising CO_2 capture adsorbent, counting on synergies between fast energy dissipation and low pressure-drop that reduce energy penalty on cyclic adsorption processes. Accordingly, the present work seeks to evaluate the applicability of a recently presented new route towards 3D-printed activated carbon combining micropores from activation and meso- and macropores from porogen templating [14], for the applicability in CO_2 capture from the post-combustion stream. Therefore, two monoliths with the same open cellular 3D printed structure and porogen templated meso- and macroporosity but varying microporosity due to differing burnoffs in the activation steps were employed in a series of fixed-bed adsorption experiments. Within these experiments, the adsorption equilibrium and the dynamic separation between CO_2 and N_2 at the temperature range between 313 and 373 K and partial pressure up to 120 kPa were studied from the respective breakthrough curves. Performance metrics such as selectivities and working capacities were also evaluated. A mathematical fixed-bed adsorption model was used to simulate the experimental data and to evaluate process performance parameters of both 3D printed activated carbons for the design of continuous cycling temperature swing adsorption process (TSA).

2. Experimental section

2.1. Materials

In this work, two CO_2-activated carbon monoliths (M1 and M2) with a tetragonal unit cell structure and a diameter of 0.008 m were studied. Two pieces of each monolith were placed in front of each other to obtain a total length of 0.084 m. The synthesis of 3D-printed activated carbon monoliths was carried out according to the method described by Steldinger et al. [14]. Briefly, a resin mixture of two monomers, 35% pentaerythritol tetraacrylate (PETA) and 35% divinylbenzene (DVB), and a porogen 30% bis(2-ethylhexyl) phthalate (DOctP) was prepared. Then, 0.4 mg mL^{-1} sudan1 (dye) and 10 mg mL^{-1} phenylbis(2,4,6-trimethylbenzoyl) phosphine oxide (BAPO; initiator) were added before the porous polymer open cell structure was produced by stereolithographic 3D printing. After that, the porogen phase and the dye were extracted by soxhlet extraction using acetone. In the final step, the resultant polymer open cell structure was stabilized by a thermal treatment in the air (at 573 K for 6 h), pyrolyzed in nitrogen (at 1173 K for 0.3 h) and activated in CO_2 (at 1133 K). The only difference between monoliths M1 and M2 is the activation time, being 6 h for M1 and 12 h for M2. The adsorbates and inert gases were supplied by Air Liquide with the following purities: He (99.9998%), CO_2 (99.998%), and N_2 (99.999%).

2.2. Characterization

The textural properties were determined using physisorption analysis with nitrogen at 77.4 K. The measurements were performed employing a BELSORP-maxII apparatus (Microtrac Retsch GmbH). Beforehand, the samples were degassed at 250 °C for 4 h under fine vacuum. The characteristic surface area was calculated applying the Brunauer-Emmett-Teller (BET) multi-point method considering five appropriate data points. Pore size distributions, the QSDFT surface area and the pore volume were deduced by applying the QSDFT adsorption model for carbon with a combined slit- and cylindrical pore geometry (fitting errors <0.2%, VersaWin Vers. 1.0). Mercury porosimetry was performed using a combined Belpore LP/HP (Microtrac Retsch GmbH) in the pressure range from 0.013 to 400 MPa. The samples were outgassed at 200 °C overnight at atmospheric pressure. Pore size distributions were calculated based on the intrusion data from 1 to 400 MPa using a cylindrical pore model after cut-off of inter particle voids at pressures below 1 MPa and compressibility correction.

2.3. Breakthrough apparatus and experimental procedure

The single-component adsorption of CO_2 and N_2 on monoliths M1 and M2 were studied in a fixed-bed apparatus [10]. The apparatus consists of three sections, namely the gas preparation section, adsorption section, and analytical section. In the gas preparation section, CO_2 or N_2 partial pressure is balanced with inert helium (He) up to 120 kPa to be introduced in the adsorption column. In the adsorption section, an adsorption column (stainless steel) dimension of 0.01 m internal diameter and 0.1 m length is located inside the oven of SRI 8610C (Gas Chromatograph equipment - USA) with controlled temperature. After measurement of partial pressure (CO_2 or N_2 balanced with inert He) the gas is sent to the adsorption column into a given constant temperature (313, 343, or 373 K). The outlet gas goes directly to the Thermal Conductivity Detector (TCD), which will evaluate the specie conductivity. Helium is used as a reference gas in the TCD analyses.

To maintain the material fixed inside the column the whole monolith is covered with glass wool and the void volume inside the column is filled with glass spheres. The monolith diameter is somewhat lower than the column inner diameter, being necessary a thin layer of glass wool to fix the monolith in the column. Before the first run, the adsorption column is activated for 12 h at 475 K under pure He flows (10 NmL/min). Between the runs, the column is heated up to 455 K and cooled up to the experiment temperature (±5 K/min) under pure He flows (20 NmL/min) to keep the column clean for the next run.

The equilibrium loading is obtained by integrating the molar flow profiles of the breakthrough curves by the following equation,

$$q_{exp,i} = \frac{1}{m_{ads}}\left(F_{fi}t_n - \int_0^{t_\infty} F_i\, dt - \varepsilon_b V_c C_{0i}\right) \quad (1)$$

where m_{ads} is the adsorbent mass, F_{fi} is the feed molar flow rate of component i at the inlet of the bed, F_i is the molar flow rate of component i at the outlet of the bed, t_∞ is the saturation time, ε_b is the bed porosity, V_c is the column adsorption volume, and C_{0i} is the feed gas-phase concentration at the inlet of the fixed bed.

The apparatus is designed to perform single or multi-component experiments, thus the dynamic separation of CO_2 and N_2 is also studied by adsorption-desorption experiments. In the gas preparation section, two synthetic gas mixture, namely (i) CO_2/N_2 (15/85 vol%), and (ii) CO_2/N_2 (50/50 vol%), at 100 kPa was set to goes through the adsorption column at three temperatures 313, 343, and 373 K. Before each experiment, the adsorption column is saturated with pure N_2 at 100 kPa. During the experiment, the outlet gas goes to a VICI Valco 6-way valve, which in determined time change its position to send a sample, trapped in the loop (1 mL), to a chromatography column (HayeSep N packed column, 24 g, and mesh 80/100) at 373 K before goes to TCD to be analyzed. The chromatographic peaks are quantified via a conductivity measurement (TCD), and the final loading is calculated by Eq. (1). After the adsorption step is finished, the desorption step is started by closing the flow rate of CO_2. The flow rate of N_2 on the desorption step is equal to the adsorption step. The outlet gas is analyzed with the same procedure described above until the column is completely cleared.

To evaluate the regenerability of adsorbent materials a set of six adsorption-desorption experiments was carried out. The adsorption experiments start at the same condition, namely a synthetic mixture of 15% CO_2 and 85% N_2 at 100 kPa and 313 K. At the end of the adsorption step, the column is completely cleared under constant N_2 flow and heating, to ensure that there is no permanent CO_2 in the column to the next adsorption cycle.

2.4. Adsorption equilibrium model

To describe the adsorption equilibrium behavior of CO_2 and N_2 on the monoliths, the dual-site Langmuir model (DSL) was used to fit the experimental data. This model (Eq. (2)) is commonly used for adsorbents where a certain degree of energy surface heterogeneity interaction adsorbate-adsorbent is expected [26],

$$q^* = q_{m1,i}\frac{b_{1i}p_i}{1+b_{1i}p_i} + q_{m2,i}\frac{b_{2i}p_i}{1+b_{2i}p_i} \quad (2)$$

where $q_{m1,i}$ and $q_{m2,i}$ are the maximum adsorbed concentration of component i in each site, b_{1i} and b_{2i} are the adsorption affinity constant of component i in each site.

The effect of temperature on the adsorption affinity constant, b_i is taken into account by the van't Hoff expression,

$$b_i = b_{\infty,i}e^{\left(\frac{-\Delta H_i}{RT}\right)} \quad (3)$$

where $b_{\infty,i}$ is the pre-exponential factor of the affinity constant at infinite temperature, R is the ideal gas constant, $(-\Delta H_i)$ is the heat of adsorption, and T is the temperature.

The extended DSL model isotherm was used to predict the interaction of binary mixture CO_2/N_2 systems by the following equation,

$$q_i^* = q_{m1,i}\frac{b_{1i}p_i}{1+\sum_{j=1}^{n} b_{1j}p_j} + q_{m2,i}\frac{b_{2i}p_i}{1+\sum_{j=1}^{n} b_{2j}p_j} \quad (4)$$

2.5. Performance metrics

Two important performance metrics used to rank adsorbents are the selectivity and working capacity. Although these performance metrics do not take into account mass and heat transfer effects, cycle configurations, and pressure drop effects, as addressed by Rajagopalan et al. [7], they still are a simple way to have a first impression of the adsorbent behavior.

The selectivity (S) of CO_2 over N_2 can be evaluated by Eq. (5) [7,27],

$$S = \left(\frac{q_{CO_2}^*}{y_{CO_2}}\right)\Big/\left(\frac{q_{N_2}^*}{y_{N_2}}\right) \quad (5)$$

where $q_{CO_2}^*$ and $q_{N_2}^*$ are the equilibrium loading of CO_2 and N_2, respectively; y_{CO_2} and y_{N_2} are the molar fraction of CO_2 and N_2, respectively. Eq. (5) can be used to predict pure selectivity (S_P) or competitivity selectivity (S_C), in which the pure or competitive loading is calculated from Eqs. (2) or (4).

The working capacity (WC) can be estimated according to the isotherm of CO_2 in two different conditions (high and low temperature for the case of TSA or high and low pressure for the case of Pressure Swing Adsorption (PSA)) by the following equation [7,27,28],

$$WC = q_{CO_2}(T_1,P_1)^* - q_{CO_2}(T_2,P_2)^* \quad (6)$$

where $q_{CO_2}(T_1,P_1)^*$ is the CO_2 equilibrium loading at the temperature T_1 and CO_2 partial pressure P_1 in the adsorption step, and $q_{CO_2}(T_2,P_2)^*$ is the CO_2 equilibrium loading at the temperature T_2 and CO_2 partial pressure P_2 in the desorption step.

2.6. Mathematical modeling

The dynamic behavior of adsorption processes can be numerically predicted according to the mass and energy conservation laws. The mathematical model employed for the simulation of the breakthrough curves in this work includes both the effect of axial dispersion and mass transfer resistances. The sorbates adsorption kinetics is taken into account by the linear rate driving force model (LDF) [29–31]. The set of coupled partial and algebraic differential equations that represent the fixed bed adsorption model are summarized in Table 1 and the respective initial and boundary conditions are summarized in Table S3 in Supporting Information (SI).

For the solution of the model, the set of coupled partial and algebraic differential equations are reduced into a system of ordinary and algebraic differential equations by the method of the lines [32]. Orthogonal Collocation method was applied to discretize the spatial coordinate [33]. The computation of the collocation points was determined by the position on the spatial coordinate using Jacobi polynomial, $P_{N^{(\alpha,\beta)}}(x)$, with $\alpha = 0$ and $\beta = 0$. The approximation of the first and second derivatives was made by collocation matrices routines $A_{i,j}$ and $B_{i,j}$,

Table 1
Mathematical model equations for fixed-bed adsorption simulation.

Phenomenon model	Equations	
ideal gas	$C = \frac{P}{RT}$	(7)
overall mass balance	$\frac{\partial F}{\partial z} + \varepsilon_b\frac{\partial C}{\partial t} + \rho_p(1-\varepsilon_b)\sum_{i=1}^{n}\frac{\partial \overline{q}_i}{\partial t} = 0$	(8)
component mass balance	$-\varepsilon_b D_{ax}\frac{\partial}{\partial z}\left(C\frac{\partial y_i}{\partial z}\right) + \frac{\partial (Fy_i)}{\partial z} + \varepsilon_b\frac{\partial (Cy_i)}{\partial t} + \rho_p(1-\varepsilon_b)\frac{\partial \overline{q}_i}{\partial t} = 0$	(9)
mass transfer rate	$\frac{\partial \overline{q}_i}{\partial t} = K_{LDF}(q^* - \overline{q}_i)$	(10)
gas-phase energy balance	$-K_{ax}\frac{\partial^2 T}{\partial z^2} + Fc_{pg}\frac{\partial T}{\partial z} + C\varepsilon_b C_{pg}\frac{\partial T}{\partial t} + (1-\varepsilon_b)a_p h_p(T - T_s) + a_c h_w(T - T_w) = 0$	(11)
solid-phase energy balance	$C_{ps}\frac{\partial T_s}{\partial t} = a_p h_p(T - T_s) + \rho_p\sum_{i=1}^{n}(-\Delta H_{st,i})\frac{\partial \overline{q}_i}{\partial t}$	(12)
isotherm model (DSL)	$q_i = \frac{q_{m1}b_{1i}p_i}{1+\sum_{j=1}^{n}b_{1j}p_j} + \frac{q_{m2}b_{2i}p_i}{1+\sum_{j=1}^{n}b_{2j}p_j}$	(4)

respectively. Thus, the system of ordinary differential equations has been solved using ode15s, a stiff ODE solver available in the MATLAB library [34], and the algebraic differential equations were solved by Gauss elimination. Twenty-five special collocation points appeared to give satisfactory accuracy and stability to the numerical solution. The solution has been implemented on a personal computer.

3. Results and discussion

3.1. Adsorbent properties and characterization

The synthesis method of the 3D-printed activated carbons allows to control the structure ranging from the mm to the nm scale, which was characterized by nitrogen physisorption analysis and Hg porosimetry. The results are summarized in Fig. 1 and Table 2. As indicated by Fig. 1a for a piece of monolith M1, the macroscopic size and shape of the activated carbon is determined by the computer designed structure (Fig. S1), while on the nm level, the porosity can be varied via the CO_2 activation conditions. By increasing the activation time at a temperature of 1133 K from 6 to 12 h, the burnoff almost linearly scales from 14 wt% to 26 wt%. The partial oxidation of the monoliths leads to a distinct rise of the nitrogen uptake for monolith M2 (12 h activated monolith) in the low-pressure region of the adsorption branch ($p/p_0 < 0.1$) compared to M1 (6 h activated monolith), indicating the creation of additional microporosity (Fig. 1b). The prolonged activation equally increases the specific surface area and pore volume for monolith M2 (QSDFT: 1307 $m^2\ g^{-1}$; 0.52 $cm^3\ g^{-1}$) compared to M1 (QSDFT: 1048 $m^2\ g^{-1}$; 0.39 $cm^3\ g^{-1}$) by ca. 30%.

Table 2
Adsorbent properties.

Monolith	M1[a]	M2[a]
Burnoff, wt.-%	14	26
Dry (total) mass, g	1.94	1.66
Total length, m	0.084	0.084
Diameter, m	0.008	0.008
Characteristic BET-surface area, m^2/g	805	1078
QSDFT surface area, m^2/g	1048	1307
Pore volume, cm^3/g	0.39	0.52
Hg-intruded volume, cm^3/g	0.15	0.18

[a] Each monolith consists of two individual pieces resulting in the respective total mass and length.

According to the pore size distributions shown in Fig. 1c, the largest gain can be attributed to micropores with a diameter less than ca. 1.5 nm. In accordance, the Hg porosimetry data reveal a similar pore size range but a ca. 20% higher intruded volume for M2 (0.18 $cm^3\ g^{-1}$) compared to M1 (0.15 $cm^3\ g^{-1}$). In other words, the CO_2 activation can be utilized to introduce additional micropores without leading excessive altering of the meso-to macroporosity. Apart from this, it should be mentioned that both activated monoliths were stable and could be normally handled in the lab.

3.2. Adsorption equilibrium

To set-up the adsorption isotherms of CO_2 and N_2 in the 3D-printed activated carbons a series of breakthrough curves on the respective

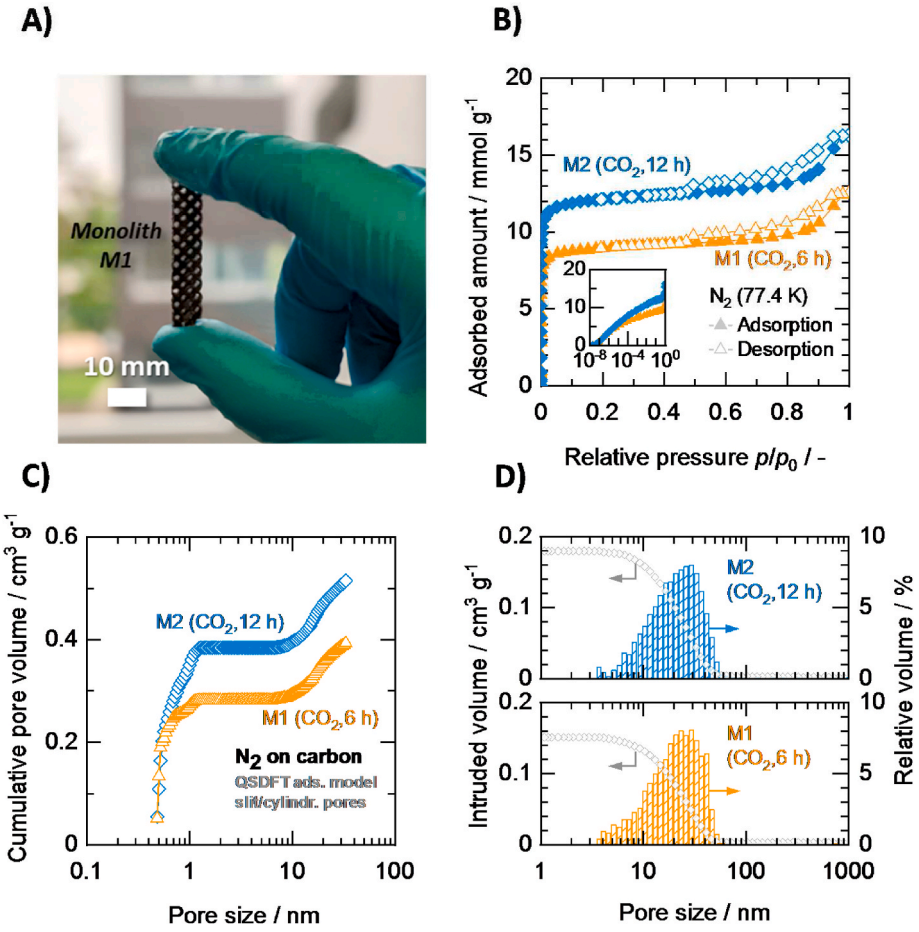

Fig. 1. A) Single piece of monolith M1; Low-temperature N_2 physisorption analysis: B) ad- (closed symbols) and desorption (open symbols) isotherm for M1 and M2 in linear and log-scale (inset); C) Cumulative pore volume derived from the nitrogen sorption data assuming a combined slit- and cylindrical pore model (QSDFT adsorption kernel); D) Cumulative and relative intruded Hg volume.

monoliths M1 and M2 were measured at three temperatures, 313, 343, and 373 K, and partial pressures up to 120 kPa. The experimental conditions are summarized in Tables S1 and S2 in the Supporting Information (SI). Fig. 2a–d shows the observed experimental breakthrough curves (symbols) at 313 K plotted in terms of normalized molar fraction y_i/y_{i0} against moles fed per unit mass of monolith M1, for components CO_2 (a), and N_2 (b), and of monolith M2 for components CO_2 (c), and N_2 (d). All the breakthrough curves observed for CO_2 and N_2 on monoliths M1 and M2 at 343 and 373 K are shown in Figs. S2–S5 of the SI. It is clear from Fig. 2a that the moles fed to reach the breakthrough of CO_2 are much higher than in the case of N_2 (Fig. 2b) on monolith M1. Consequently, the equilibrium loading for CO_2 and N_2 is 1.74 and 0.23 mol/kg, respectively, which means that the sorption uptake of CO_2 is almost 7.56 times higher in CO_2 than in N_2 (Run 1.3). The same trend was observed on monolith M2 (Fig. 2c and d) and also at the other experimental conditions. Moreover, as the partial pressure increases the moles fed to reach breakthrough increases which indicate that data is thermodynamically consistent (the loadings of CO_2 and N_2 in both monoliths were obtained by applying Eq. (1)).

Fig. 3 shows the experimental (symbols) and theoretical (lines) isotherms measured for CO_2 and N_2 on monoliths M1 (closed symbols) and M2 (open symbols) at (a) 313, (b) 343, and (c) 373 K from the breakthrough curves. As can be seen from Fig. 3a, CO_2 loading on monolith M1 (3.0 mol/kg) is slightly lower than monolith M2 (3.18 mol/kg), especially at the higher partial pressure (>50 kPa) and lower temperature (313 K). For the other temperatures, the loading of CO_2 is practically the same on both monoliths (Fig. 3b and c). In the case of N_2 (Fig. 3a–c), the loading reached on monolith M2 is higher than in monolith M1 at all temperatures studied. Monoliths M1 and M2 were activated under a CO_2 atmosphere at 1133 K for 6 and 12 h, respectively. The specific surface area and pore volume increased with the increase of CO_2 activation time (Table 2). Additionally, the monolith narrow micropores are widened, as activation proceeds, being more accessible for N_2 which can justify the increased N_2 loading on monolith M2. In contrast, the widened monolith M2 narrow micropores have a negative effect to "trap" CO_2 at low partial pressure (as can be seen in Fig. 3a). This effect has been also observed by Querejeta et al. [22] who have studied CO_2, N_2, O_2, and H_2O on two carbon honeycomb monoliths with different burn-off degrees.

Table 3 shows the dual- and single-site Langmuir parameters calculated from the fitting of the adsorption equilibrium data for CO_2 and N_2 shown in Fig. 3, respectively. The lines in Fig. 3 clearly show that the isotherm model describes well the equilibrium data. The heat of adsorption for CO_2 varies between −40 and −20 kJ/mol on M1, and –24.7 to −22.5 kJ/mol on M2. For N_2, the heat of adsorption obtained on M1 is equal to −16 kJ/mol, and on M2 is equal to −13 kJ/mol. The heats of adsorption obtained in this work are within the range reported to similar materials, namely, AC monolith [22,25] and hybrid (AC/zeolite) [27] monolith.

3.3. Kinetics of sorption

For each experimental condition (feed composition, gas velocities, temperatures, and pressures), the values of the transport parameters were obtained by commonly used correlations as summarized in Table S4 in the SI. As an exception, the mass transfer coefficient (K_{LDF}) was obtained from a "trial-and-error" procedure by applying the linear driving force model (LDF) to the mass transfer rate equation to obtain the best fit of the breakthrough curves. The sum squares errors between the experimental breakthrough and the simulated breakthrough, $\sum_{i=0}^{t_\infty} (y_{exp}(t_i) - y_{sim}(t_i))^2$, was used as an objective function to optimize the K_{LDF} coefficient. Fig. 4 compares the experimental (symbols) and simulated (lines) breakthrough curves on monoliths (a) M1 and (b) M2 for a feed composition of CO_2/N_2 (15/85 vol %) at 313 K. As can be seen by the lines in Fig. 4a and b, the simulation results with K_{LDF} around 0.070 s^{-1} in the case of monolith M1 and 0.075 s^{-1} in the case of monolith M2 are in good agreement with experimental data. It is worth mentioning the difference between K_{LDF} (0.070 s^{-1} and 0.075 s^{-1}), for this set of experiments, is not significant in the simulation. Thus, this

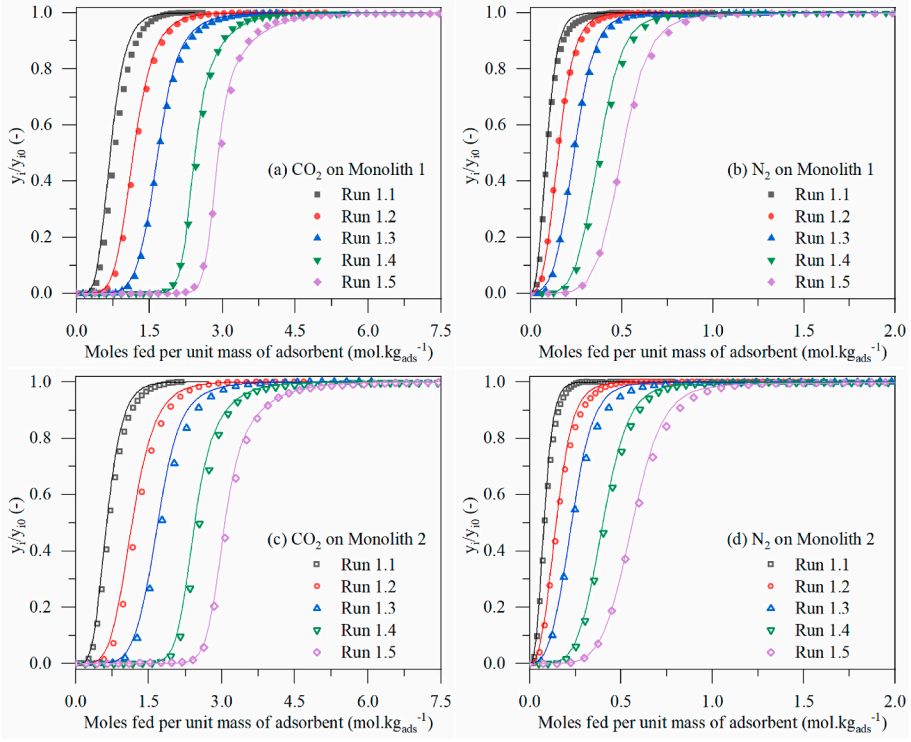

Fig. 2. Experimental and numerical breakthrough curves of CO_2 (a), and N_2 (b) on Monolith 1 (closed symbols), and to CO_2 (c), and N_2 (d) on Monolith 2 (open symbols) at 313 K. Experimental = symbols; Numerical = lines.

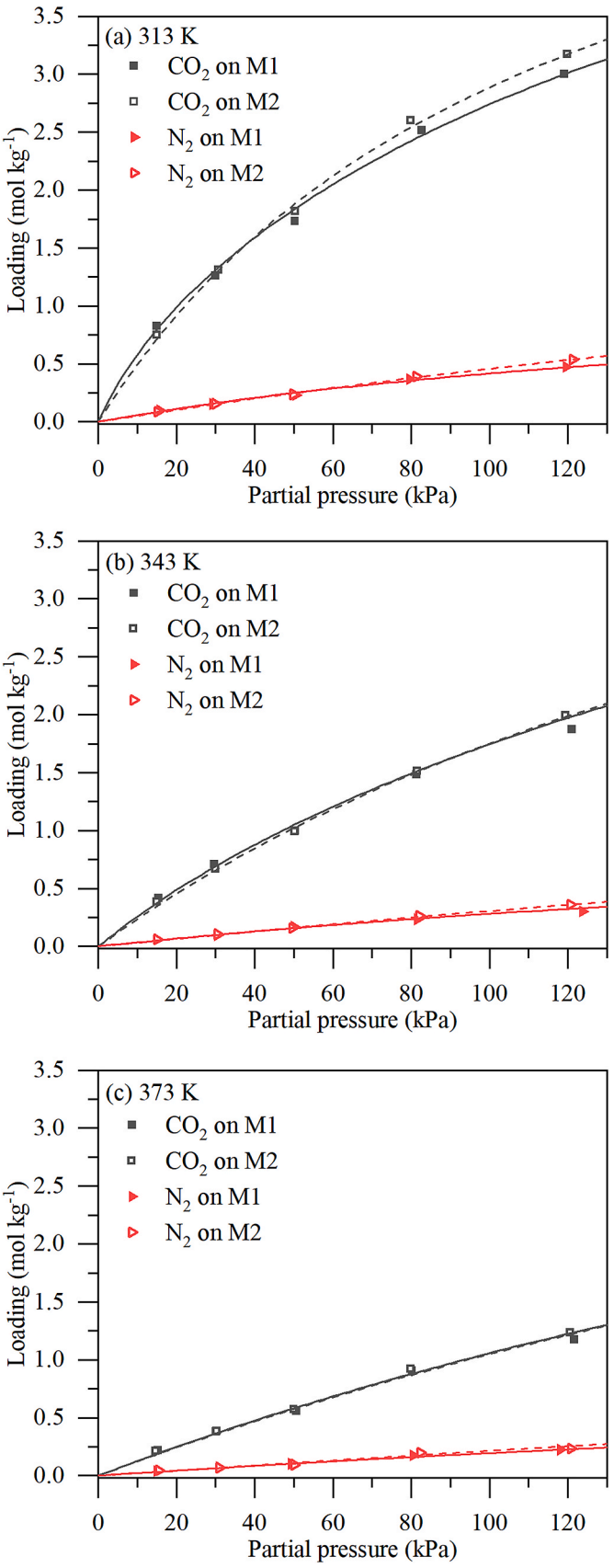

Fig. 3. Adsorption equilibrium isotherms of CO_2 and N_2 on M1 (closed symbols) and M2 (open symbols) at 313 (a), 343 (b), and 373 K (c). Experimental = symbols; Numerical = lines.

Table 3
Adsorption equilibrium model parameters for sorption of CO_2 and N_2 on monoliths M1 and M2.

Species	Monolith	q_m (mol/kg)		b (1/kPa)[a]		(ΔH) (kJ/mol)	
		$q_{m,1}$	$q_{m,2}$	b_1	b_1	$(\Delta H)_1$	$(\Delta H)_2$
CO_2	1	0.75	5.95	5.77×10^{-2}	0.55×10^{-2}	−40.0	−20.1
	2	3.07	3.33	1.05×10^{-2}	0.65×10^{-2}	−22.5	−24.7
N_2	1	1.29	–	0.48×10^{-2}	–	−16.0	–
	2	2.99	–	0.18×10^{-2}	–	−13.7	–

[a] The reference temperature used is 313 K.

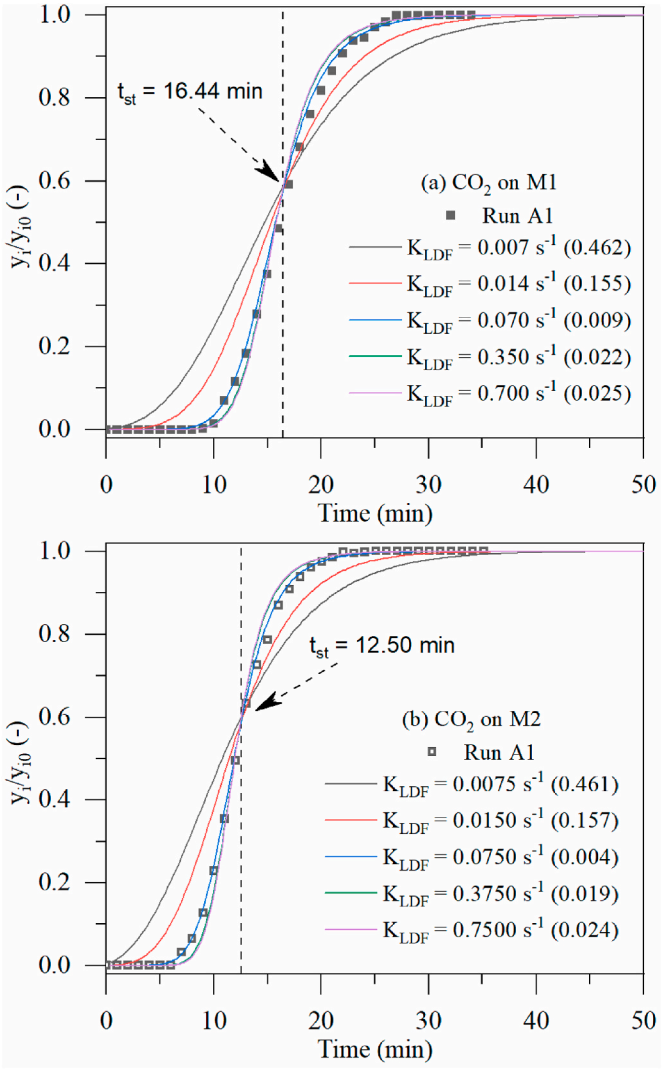

Fig. 4. Kinetic coefficient effects on numerical breakthrough curves of CO_2 on (a) M1, and (b) M2 at 313 K. Dashed lines indicate the CO_2 stoichiometric time; Experimental = symbols; Numerical = lines. Sum squares of error were shown in brackets.

result points out that the activation time has a minor influence on the mass transfer rate for CO_2 and N_2 since the K_{LDF} reported for both monoliths is close to each other. These values were used to predict the desorption breakthrough curves, addressed in the next section. The same procedure was applied for the simulation of all breakthrough curves shown in this work. The resume of the model simulation parameters for

the single and binary experiments are summarized in Tables S5 and S6 (single), and S8 (binary) on the SI.

In Fig. 4a and b, the dashed line indicates the CO_2 stoichiometric time of each run, being 16.44 min in monolith M1 (a) and 12.50 min on monolith M2 (b). The stoichiometric time is derived through an overall mass balance of an adsorption column in equilibrium with the adsorbate [29,35],

$$t_{st} = \frac{L}{v_i}\left(1 + \frac{\rho_b q_0}{\varepsilon_b C_0}\right) \tag{13}$$

where v_i is the interstitial velocity, L is the column length, ε_b is the bed porosity, ρ_b is the bulk density, q_0 is the adsorbed concentration in equilibrium with the gas phase concentration c_0 at the column feed condition.

As can be seen in Fig. 4a and b, the experimental and simulated breakthrough curves cross the stoichiometric time at the same point, indicated by an arrow in Fig. 4a and b, which is around 50–60% of the breakthrough curves. This effect is expected since the resistance to mass transfer must respect the stoichiometric time. In other words, for values of K_{LDF}, in which the simulator provides consistent results, the breakthrough curves must always pass through the stoichiometric point. Thus, when the simulator is submitted to different values of K_{LDF}, the expected response is more dispersed curves for lower K_{LDF} values and less dispersed curves for higher K_{LDF} values. These effects are similar to the results presented by Lapidus and Amundson [36], which evaluate for the first time the effect of longitudinal diffusion in chromatography and ion exchange fixed-bed columns.

Concerning a comparison with other works, Zhao et al. have reported kinetic coefficients (K_{LDF}) of 0.100 s^{-1} at 293 K for a carbon monolith [37], and 0.120 s^{-1} at 298 K for a hybrid monolith (H-ZSM5/activated carbon) [27], for a feed gas mixture of 15% CO_2 balanced with N_2, which are in the same range of the values reported in this work.

3.4. Binary adsorption

For the binary separation studies, it was considered two different ratio gas mixtures: (i) CO_2/N_2 (15/85 vol%), and (ii) CO_2/N_2 (50/50 vol %), at a constant total pressure of 100 kPa and three temperatures 313, 343, and 373 K. All the runs studied, started from a column saturated with pure N_2 at 100 kPa. The desorption of the fixed bed was also carried out with pure N_2 at the same total flow rate value used in the adsorption step. The experimental conditions are summarized in Table S7 in the SI. Figs. 5 and 6 show the adsorption and desorption breakthrough curves on monolith M1 and Figs. 7 and 8 on monolith M2.

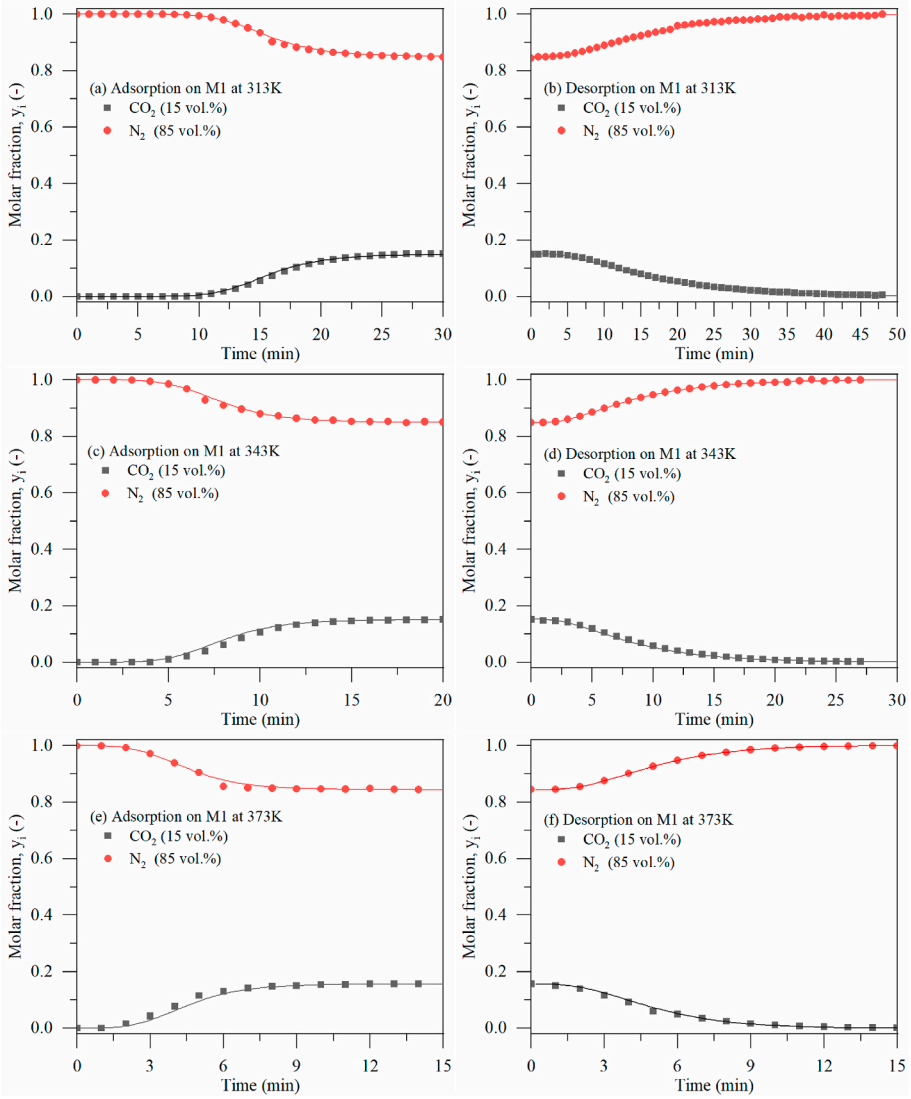

Fig. 5. Adsorption and desorption breakthrough curves for a mixture ratio CO_2/N_2 (15/85 vol %) on Monolith 1 at (a–b) 313 K, (c–d) 343 K, and (e–f) 373 K. The column is first saturated with N_2 (100 kPa), and then, it is fed a gas mixture. Experimental = symbols; Numerical = lines.

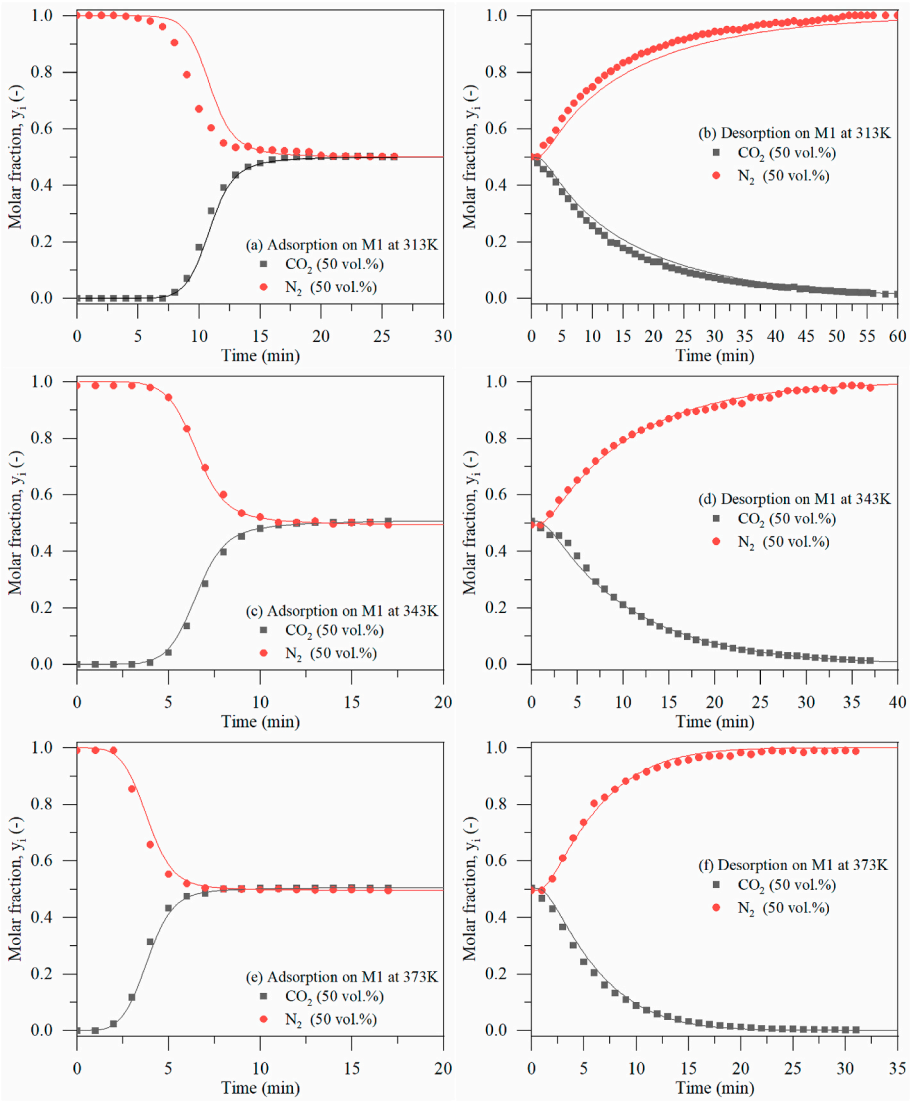

Fig. 6. Adsorption and desorption breakthrough curves for a mixture ratio CO_2/N_2 (50/50 vol %) on Monolith 1 at (a–b) 313 K, (c–d) 343 K, and (e–f) 373 K. The column is first saturated with N_2 (100 kPa), and then, it is fed a gas mixture. Experimental = symbols; Numerical = lines.

As can be seen in Fig. 5a, for the experiment with the mixture ratio CO_2/N_2 (15/85 vol%), at 313 K the CO_2 breaks the column at around 10 min (black symbols) and reaches saturation at around 25 min. Interestingly, the breakthrough time of CO_2 in the bed decreases from 10 to 2 min, as the temperature increases from 313 K (Fig. 5a) to 373 K (Fig. 5e), which indicates a strong impact of temperature on the CO_2 sorption uptake. Regarding the desorption curves (Fig. 5b), the CO_2 concentration decreases slowly, and hence, the complete cleaning of the bed from CO_2 takes around 45 min. This effect is expected since the isotherm of CO_2 on monolith M1 is of favorable nature for adsorption (Type I is observed in the measurement range) being unfavorable for desorption (see Fig. 3). Thus, the CO_2 desorption curves concentration waves are dispersive which requires a long time for the regeneration of the column. As the temperature increases, the time to regenerate the bed decreases from 45 min at 313 K (Fig. 5b) to 12 min at 373 K (Fig. 5f), since the equilibrium loading of CO_2 is lower as the temperature increases. For the mixture ratio 50/50 (Fig. 6), the breakthrough curves become steeper due to the higher concentration of CO_2 in the feed leading to a higher compression of the concentration wave fronts. Regarding the adsorption and desorption of CO_2 on monolith M2 (Figs. 7 and 8), the same trends were observed.

Overall, the lines shown in Figs. 5–8, which represent the simulation results, are in good agreement with the experimental data. The simulation parameters are summarized in Table S8. It is worth mentioning that the extended multi-component DSL model was used to predict the multicomponent adsorption equilibria on both monoliths.

3.5. Regenerability and performance metrics

To assess the monolith's feasibility to be renewed and reused over several adsorption/desorption cycles, six cycles were carried out for a mixture of CO_2/N_2 (15/85 vol %) at 100 kPa and 313 K. Fig. S6 in the SI shows the loading of CO_2 in both monoliths is stable. It is worth mentioning that the initial condition from one experiment to another shows a tiny difference (see Table S9 on SI) which can explain the slight difference between the loadings for the same monolith. In general, both monoliths show excellent stability and regenerability over consecutive cycles performed in this work.

The CO_2 working capacity (Eq. (6)) was calculated for several combinations of regeneration temperature and desorption pressure. The loadings of CO_2 were obtained from the extended DSL isotherm taking into account the competitive interaction with N_2. The adsorption capacity, $q^*_{ads} = q(293\,K,\ 15kPa)$, was calculated at a fixed condition of 15% CO_2 and 85% N_2 at 293 K and 100 kPa. The desorption capacity,

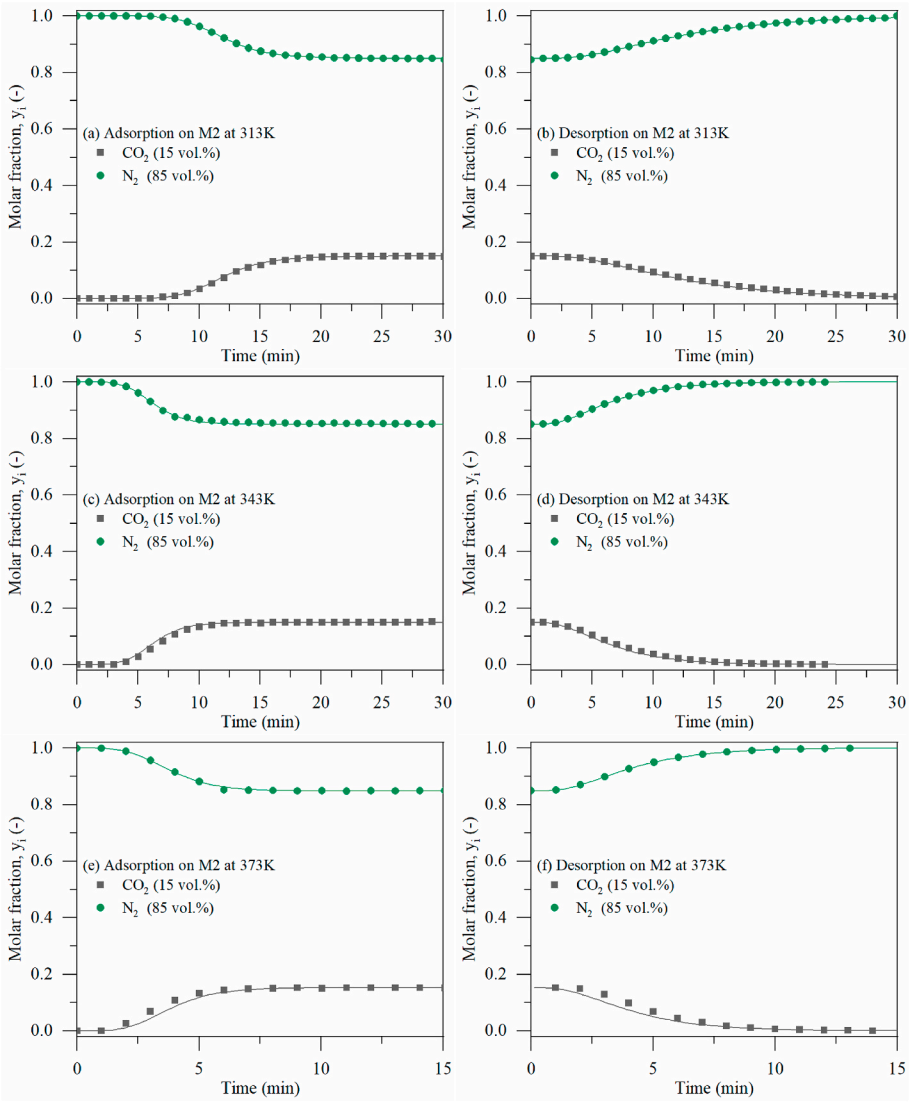

Fig. 7. Adsorption and desorption breakthrough curves for a mixture ratio CO_2/N_2 (15/85 vol %) on Monolith 2 at (a–b) 313 K, (c–d) 343 K, and (e–f) 373 K. The column is first saturated with N_2 (100 kPa), and then, it is fed a gas mixture. Experimental = symbols; Numerical = lines.

$q^*_{des} = q(T_2,\ P_2)$, was calculated taking into account a range of CO_2 pressure between 1 and 100 kPa and a range of temperature from 293 to 473 K.

Fig. 9 shows the contours of the CO_2 working capacity for monoliths M1 and M2 as a function of different regeneration temperatures and pressures. As expected, the working capacity increase as desorption pressure decrease and regeneration temperature increase for both monoliths. For monolith M1 (Fig. 9a) keeping the desorption pressure at 15 kPa the working capacity increase from 0.15 to 0.90 mol/kg as regeneration temperature increase from 300 to 354 K (see the gray dashed lines in Fig. 9a). This result shows that the 3D-printed activated carbon can be explored in a temperature swing adsorption process due to a great increase in the WC with a small change in the regeneration temperature. In the case of monolith M2, considering the same conditions, the WC does not reach 0.75 mol/kg, as seen in Fig. 9b. This can be explained due to the N_2 being more adsorbed on M2 than M1, which results in a negative effect on the performance metrics of M2. As shown by Rajagopalan et al. [7], the affinity of N_2 can play a critical role in deciding the process performance for post-combustion CO_2 capture. In our study, N_2 has more affinity with monolith M2 due to a higher burnoff during activation, which increase the specific area and pore volume accessible to N_2 molecules and thus harms the performance. In contrast, the monolith M1 has a better performance WC as the affinity of N_2 is lower. Besides, two other advantages come from the lower activation time, namely, the reduction of the manufacturing cost and increase of the product yield.

The CO_2 selectivities over N_2 calculated from Eq. (5), considering the binary interaction, are 18 and 10 for monoliths M1 and M2, respectively. These values were calculated from isotherm parameters considering a mixture of CO_2 15% and N_2 85% at 100 kPa and 313 K. For similar materials, the selectivity values obtained in this work are within the range reported in the literature [22,38].

4. Conclusions

In this work, the potential of two 3D-printed activated carbons with different activation times (M1<M2) has been investigated for their use in CO_2 capture in post-combustion streams. A series of fixed-bed breakthrough adsorption experiments were performed in a wide range of temperature and pressure of interest for post-combustion applications, namely: between 313 and 373 K and the partial pressure up to 120 kPa. The adsorption equilibrium and heat of adsorption in both monoliths follow the order $CO_2 \gg N_2$. The isotherm Langmuir model was used to predict the N_2 adsorption equilibrium and dual-site Langmuir model

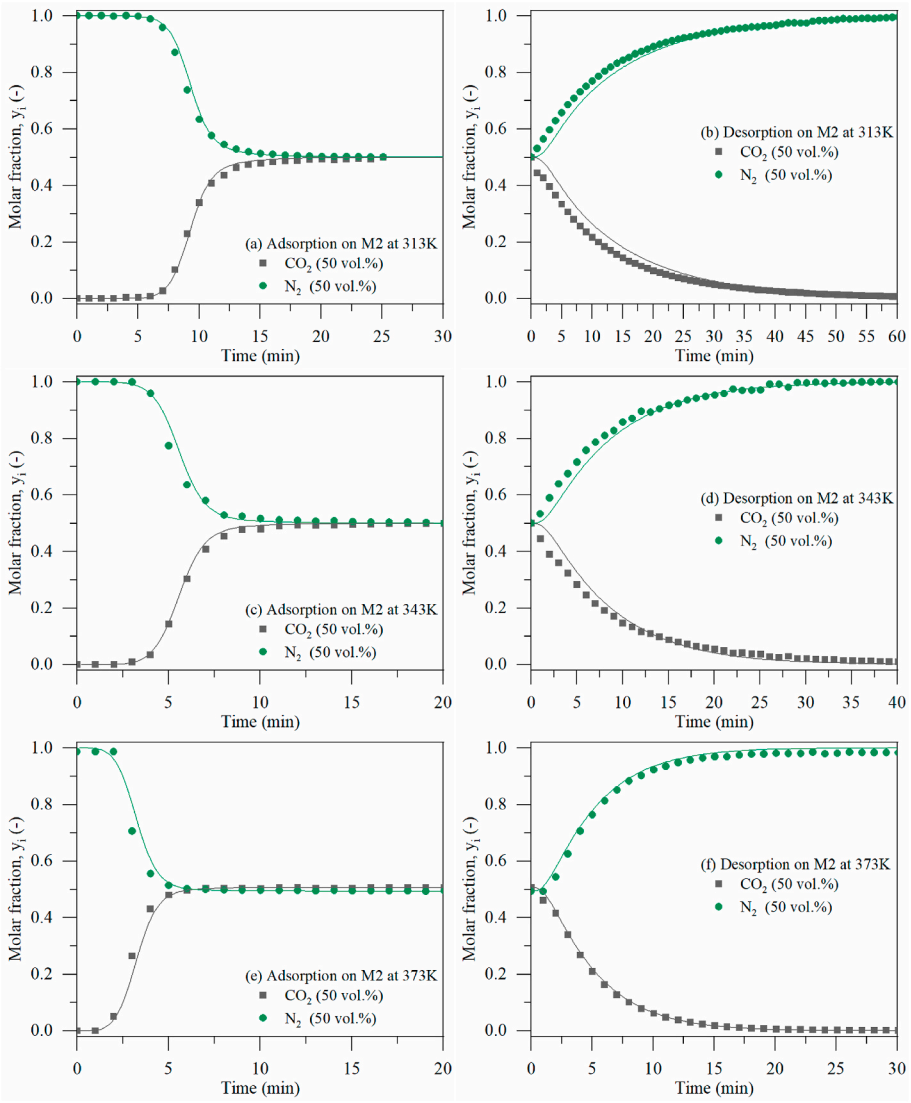

Fig. 8. Adsorption and desorption breakthrough curves for a mixture ratio CO_2/N_2 (50/50 vol %) on Monolith 2 at (a–b) 313 K, (c–d) 343 K, and (e–f) 373 K. The column is first saturated with N_2 (100 kPa), and then, it is fed a gas mixture. Experimental = symbols; Numerical = lines.

for the CO_2, both being in good agreement with the experimental data. The extended multi-component dual-site Langmuir model was used and provided a good prediction of the competitive interaction between the compounds in multicomponent breakthrough experiments. It was shown that a higher burnoff rate during the activation results in a higher specific area and pore volume. As a result of the higher specific area and pore volume, it is expected higher adsorption capacity for both components. However, the adsorption capacity of CO_2 at higher temperatures (343 and 373 K) and higher pressures (>50 kPa) is similar in both monoliths which means that the increase in the specific surface area of monolith M2 is related to microporosity only accessible to N_2 molecules. Nevertheless, as the N_2 affinity increases, a negative effect is observed on CO_2 selectivity and working capacity on monolith M2. For example, considering a typical post-combustion condition, the selectivity of CO_2 over N_2 is 18 for M1 and 10 for M2. In the case of CO_2 working capacities, the monolith M1 has a better performance than M2 at the same range of regeneration temperature. Both materials presented excellent stability and regenerability over consecutive adsorption-desorption experiments. The mathematical model used in this work describes well the adsorption and desorption breakthrough curves data. Finally, the present work indicates that the 3D-printed activated carbon can be used in a temperature swing adsorption process for CO_2 capture.

CRediT authorship contribution statement

Lucas F.A.S. Zafanelli: Writing – original draft, Software, Investigation, Formal analysis. **Adriano Henrique:** Writing – review & editing, Software, Investigation, Formal analysis. **Hendryk Steldinger:** Writing – review & editing, Validation, Investigation. **Jose L. Diaz de Tuesta:** Writing – review & editing, Validation, Project administration, Funding acquisition. **Jan Gläsel:** Writing – review & editing, Software, Investigation, Formal analysis. **Alírio E. Rodrigues:** Writing – review & editing, Visualization, Validation, Supervision, Project administration, Funding acquisition. **Helder T. Gomes:** Writing – review & editing, Visualization, Validation, Supervision, Project administration, Funding acquisition. **Bastian J.M. Etzold:** Writing – review & editing, Visualization, Validation, Supervision, Resources, Project administration, Funding acquisition. **José A.C. Silva:** Writing – review & editing, Visualization, Validation, Supervision, Resources, Project administration, Funding acquisition.

Declaration of competing interest

The authors declare that they have no known competing financial interests or personal relationships that could have appeared to influence

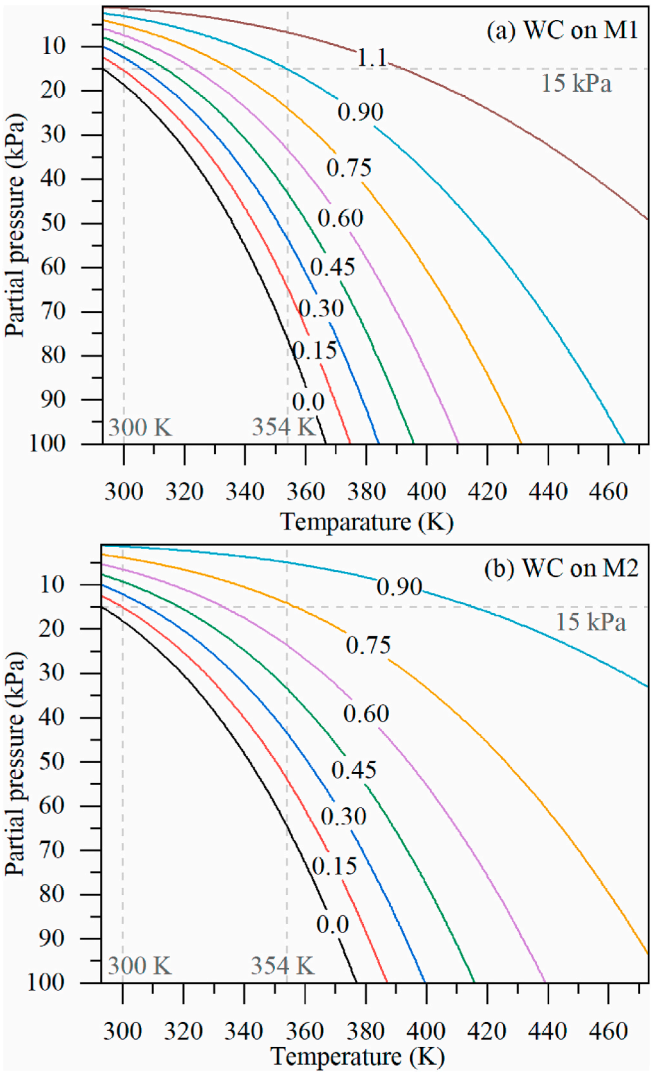

Fig. 9. Contours of CO_2 working capacity (WC) for monoliths (a) M1, and (b) M2 as a function of several combinations of regeneration temperature and pressure.

the work reported in this paper.

Appendix A. Supplementary data

Supplementary data to this article can be found online at https://doi.org/10.1016/j.micromeso.2022.111818.

Nomenclature

a_p	Specific area of the pellet (m^{-1})
a_c	Specific area of the column (m^{-1})
b_i	Adsorption equilibrium constant of component i (kPa^{-1})
$b_{\infty,i}$	Pre-exponential factor of the affinity constant at infinite temperature of component i (kPa^{-1})
C	Total gas concentration (mol m^{-3})
C_f	Feed gas concentration (mol m^{-3})
C_{pg}	Heat capacity of gas (J mol^{-1} K^{-1})
C_{ps}	Heat capacity of solid (J mol^{-1} K^{-1})
d_b	Beads diameter (m)
d_c	Column diameter (m)
D_{ax}	Axial mass dispersion coefficient (m^2 s^{-1})
D_m	Molecular diffusivity (m^2 s^{-1})
D_p	Effective Macropore diffusivity (m^2 s^{-1})

Acknowledgments

Generally, the authors are thankful to Dr. M. Rückriem and Dr. A. Schreiber from Microtrac Retsch GmbH for the kind support with nitrogen physisorption and mercury porosimetry measurements.

The authors acknowledge the joint financial support from Fundação para a Ciência e a Tecnologia (FCT), in Portugal, and the Deutscher Akademischer Austauschdienst (DAAD), in Germany. Foundation for Science and Technology (FCT, Portugal) and ERDF under Programme PT2020 to CIMO (UIDB/00690/2020) and POCI-01-0145-FEDER006984-Associate Laboratory LSRE-LCM. Foundation for Science and Technology (FCT, Portugal) under Programme PTDC 2020 * 3599-PPCDTI * Engenharia dos Processos Químicos * project PTDC/EQU-EPQ/0467/2020. Foundation for Science and Technology (FCT, Portugal), through the individual research grants SFRH/BD/148525/2019 for Adriano Henrique and DFA/BD/7925/2020 for Lucas F. A. S. Zafanelli.

D_k	Knudsen diffusivity ($m^2\ s^{-1}$)
D_c	Intracrystalline diffusivity ($m^2\ s^{-1}$)
F	Total molar flux (mol $m^{-2}\ s^{-1}$)
h_p	Film heat transfer coefficient (W $m^{-2}\ K^{-1}$)
h_w	Wall heat transfer coefficient (W $m^{-2}\ K^{-1}$)
K_{LDF}	Linear Driving Force coefficient (s^{-1})
K_{ax}	Effective axial bed thermal conductivity (W $m^{-1}\ K^{-1}$)
K	Dimensionless Henry's law equilibrium constant (−)
k'	Overall effective rate coefficient (s^{-1})
k_f	Film mass transfer coefficient (m s^{-1})
L	Length of column (m)
M_i	Molecular mass of component i (kg $kmol^{-1}$)
m_{ads}	Mass of adsorbent (kg)
p_i	Partial pressure of component i (kPa)
P	Total pressure of column (kPa)
P_{em}	Peclet number (−)
q_i	Adsorbed phase concentration of component i (mol kg^{-1})
$\overline{q}_i$	Average adsorbed phase concentration of component i (mol kg^{-1})
q^*	Equilibrium adsorbed concentration of component (mol kg^{-1})
q_m	Maximum adsorbed phase concentration (mol kg^{-1})
r_c	Crystal radius (m)
R_p	Particle radius (m)
R	Universal gas constant (J $mol^{-1}\ K^{-1}$)
S_{ij}	Selectivity of component i over j (−)
t	Time (s)
t_{st}	Stoichiometric time (s)
T	Temperature in bulk gas phase (K)
T_s	Temperature in solid phase (K)
T_w	Column wall temperature (K)
v_i	Interstitial velocity (m s^{-1})
y_i	Molar fraction of component i (−)
z	Axial coordinate in bed (m)

Greek Letters

ΔH_i	Heat adsorption of species i (J mol^{-1})
ΔH_{st}	Isosteric heat adsorption (J mol^{-1})
ε_b	Bed porosity
ε_p	Particle porosity
ρ_p	Solid Density (kg m^{-3})
ρ_s	Apparent adsorbent density (kg m^{-3})
ρ_b	Bulk density (kg m^{-3})
θ	$= q/q_m$

References

[1] M. Bui, C.S. Adjiman, A. Bardow, E.J. Anthony, A. Boston, S. Brown, P.S. Fennell, S. Fuss, A. Galindo, L.A. Hackett, J.P. Hallett, H.J. Herzog, G. Jackson, J. Kemper, S. Krevor, G.C. Maitland, M. Matuszewski, I.S. Metcalfe, C. Petit, G. Puxty, J. Reimer, D.M. Reiner, E.S. Rubin, S.A. Scott, N. Shah, B. Smit, J.P.M. Trusler, P. Webley, J. Wilcox, N. Mac Dowell, Energy Environ. Sci. 11 (2018) 1062–1176, https://doi.org/10.1039/c7ee02342a.

[2] S. Lawson, M. Snarzyk, D. Hanify, A.A. Rownaghi, F. Rezaei, Ind. Eng. Chem. Res. 59 (2020) 7151–7160, https://doi.org/10.1021/acs.iecr.9b05445.

[3] N. Politakos, I. Barbarin, L.S. Cantador, J.A. Cecilia, E. Mehravar, R. Tomovska, Ind. Eng. Chem. Res. 59 (2020) 8612–8621, https://doi.org/10.1021/acs.iecr.9b06998.

[4] C. Song, Q. Liu, S. Deng, H. Li, Y. Kitamura, Renew. Sustain. Energy Rev. 101 (2019) 265–278, https://doi.org/10.1016/j.rser.2018.11.018.

[5] K. Xie, Q. Fu, G.G. Qiao, P.A. Webley, J. Membr. Sci. 572 (2019) 38–60, https://doi.org/10.1016/j.memsci.2018.10.049.

[6] M.J. Regufe, A.F.P. Ferreira, J.M. Loureiro, Y. Shi, A.E. Rodrigues, A.M. Ribeiro, Adsorption 24 (2018) 249–265, https://doi.org/10.1007/s10450-018-9938-1.

[7] A.K. Rajagopalan, A.M. Avila, A. Rajendran, Int. J. Greenh. Gas Control 46 (2016) 76–85, https://doi.org/10.1016/j.ijggc.2015.12.033.

[8] J.A.C. Silva, A.F. Cunha, K. Schumann, A.E. Rodrigues, Microporous Mesoporous Mater 187 (2014) 100–107, https://doi.org/10.1016/j.micromeso.2013.12.017.

[9] L. Riboldi, O. Bolland, Int. J. Greenh. Gas Control 39 (2015) 1–16, https://doi.org/10.1016/j.ijggc.2015.02.001.

[10] L.F.A.S. Zafanelli, A. Henrique, M. Karimi, A.E. Rodrigues, J.A.C. Silva, Ind. Eng. Chem. Res. 59 (2020) 13724–13734, https://doi.org/10.1021/acs.iecr.0c01911.

[11] E. Gomez-Delgado, G. Nunell, A.L. Cukierman, P. Bonelli, Environ. Sci. Pollut. Res. 27 (2020) 13915–13929, https://doi.org/10.1007/s11356-020-07830-4.

[12] C.A. Trickett, A. Helal, B.A. Al-Maythalony, Z.H. Yamani, K.E. Cordova, O. M. Yaghi, Nat. Rev. Mater. 2 (2017) 1–16, https://doi.org/10.1038/natrevmats.2017.45.

[13] I. Sharma, D. Friedrich, T. Golden, S. Brandani, Ind. Eng. Chem. Res. 59 (2020) 7109–7120, https://doi.org/10.1021/acs.iecr.9b05337.

[14] H. Steldinger, A. Esposito, K. Brunnengräber, J. Gläsel, B.J.M. Etzold, Adv. Sci. 6 (2019) 1–9, https://doi.org/10.1002/advs.201901340.

[15] F. Rezaei, P. Webley, Separ. Purif. Technol. 70 (2010) 243–256, https://doi.org/10.1016/j.seppur.2009.10.004.

[16] X. Liu, G.J.H. Lim, Y. Wang, L. Zhang, D. Mullangi, Y. Wu, D. Zhao, J. Ding, A. K. Cheetham, J. Wang, Chem. Eng. J. 403 (2021), 126333, https://doi.org/10.1016/j.cej.2020.126333.

[17] P. Tosi, G.P.M. van Klink, C. Hurel, C. Lomenech, A. Celzard, V. Fierro, C. Delgado-Sanchez, A. Mija, Appl. Mater. Today. 20 (2020), 100622, https://doi.org/10.1016/j.apmt.2020.100622.

[18] A. Beltzung, A. Klaue, C. Colombo, H. Wu, G. Storti, M. Morbidelli, Energy Technol 6 (2018) 718–727, https://doi.org/10.1002/ente.201700649.

[19] S. Couck, J. Cousin-Saint-Remi, S. Van der Perre, G.V. Baron, C. Minas, P. Ruch, J. F.M. Denayer, Microporous Mesoporous Mater 255 (2018) 185–191, https://doi.org/10.1016/j.micromeso.2017.07.014.

[20] J. Singh, H. Bhunia, S. Basu, Environ. Technol. Innovat. 20 (2020), 101104, https://doi.org/10.1016/j.eti.2020.101104.

[21] E.M. Kutorglo, J. Kovačovič, D. Trunov, F. Hassouna, A. Fučíková, D. Kopecký, I. Sedlářová, M. Šoóš, Chem. Eng. J. 388 (2020), https://doi.org/10.1016/j.cej.2020.124308.

[22] N. Querejeta, M.G. Plaza, F. Rubiera, C. Pevida, T. Avery, S.R. Tennisson, Energy Proc. 114 (2017) 2341–2352, https://doi.org/10.1016/j.egypro.2017.03.1366.
[23] Q. Zhao, F. Wu, K. Xie, R. Singh, J. Zhao, P. Xiao, P.A. Webley, Chem. Eng. J. 336 (2018) 659–668, https://doi.org/10.1016/j.cej.2017.11.167.
[24] M.J. Regufe, A.F.P. Ferreira, J.M. Loureiro, A. Rodrigues, A.M. Ribeiro, Microporous Mesoporous Mater 278 (2019) 403–413, https://doi.org/10.1016/j.micromeso.2019.01.009.
[25] B. Verougstraete, A. Martín-Calvo, S. Van der Perre, G. Baron, V. Finsy, J.F. M. Denayer, Chem. Eng. J. 383 (2020), 123075, https://doi.org/10.1016/j.cej.2019.123075.
[26] D.D. Do, Adsorption Analysis: Equilibria and Kinetics, Imperial College Press, 1998, https://doi.org/10.1142/9781860943829.
[27] Q. Zhao, F. Wu, Y. Men, X. Fang, J. Zhao, P. Xiao, P.A. Webley, C.A. Grande, Chem. Eng. J. 358 (2019) 707–717, https://doi.org/10.1016/j.cej.2018.09.196.
[28] A. Ntiamoah, J. Ling, P. Xiao, P.A. Webley, Y. Zhai, Ind. Eng. Chem. Res. 55 (2016) 703–713, https://doi.org/10.1021/acs.iecr.5b01384.
[29] D.M. Ruthven, Principles of Adsorption and Adsorption Processes, first ed., John Wiley & Sons, New York, 1984.
[30] E. Glueckauf, J. Chromatogr. Libr. 51 (1955), https://doi.org/10.1016/S0301-4770(08)61562-6. A1–A68.
[31] S. Sircar, J.R. Hufton, A. Products (2000) 137–147.
[32] W.E. Schiesser, G.W. Griffiths, A Compendium of Partial Differential Equation Models, Cambridge University Press, Cambridge, 2009, https://doi.org/10.1017/CBO9780511576270.
[33] J. Villadsen, L.M. Michael, Solution of Differential Equation Models by Polynomial Approximation, 1978. New Jersey.
[34] L.F. Shampine, M.W. Reichelt, J. Siam, Sci. Comput. 18 (1997) 1–22.
[35] N.S. Wilkins, A. Rajendran, S. Farooq, Adsorption 27 (2021) 397–422, https://doi.org/10.1007/s10450-020-00269-6.
[36] L. Lapidus, R. Amundson, J. Phys. Chem. 56 (8) (1952) 984–988, https://doi.org/10.1021/j150500a014.
[37] Q. Zhao, F. Wu, Y. He, P. Xiao, P.A. Webley, Chem. Eng. J. 327 (2017) 441–453, https://doi.org/10.1016/j.cej.2017.06.123.
[38] D. Zabiegaj, M. Caccia, M.E. Casco, F. Ravera, J. Narciso, J. CO2 Util. 26 (2018) 36–44, https://doi.org/10.1016/j.jcou.2018.04.020.